Estimates of cortical column orientation improve MEG source inversion

James Bonaiuto, Fardin Afdideh, Maxime Ferez, Konrad Wagstyl, Jérémie Mattout, Mathilde Bonnefond, Gareth Barnes, Sven Bestmann

Estimates of cortical column orientation improve MEG source inversion

James J Bonaiuto[1,2], Fardin Afdideh[2,3], Maxime Ferez[2,3], Konrad Wagstyl[4,5], Jérémie Mattout[2,3], Mathilde Bonnefond[2,3], Gareth R Barnes[5*], Sven Bestmann[5,6*]

*: joint last author

1) Institut des Sciences Cognitives Marc Jeannerod, CNRS UMR 5229, Bron, France

2) Université Claude Bernard Lyon 1, Université de Lyon, France

3) Lyon Neuroscience Research Center, Brain Dynamics and Cognition team, INSERM UMRS 1028, CNRS UMR 5292, Bron, France

4) University of Cambridge, Department of Psychiatry, Cambridge CB2 0SZ, UK

5) Wellcome Centre for Human Neuroimaging, UCL Queen Square Institute of Neurology, University College London (UCL), London, WC1N 3BG, UK

6) Dept of Clinical and Movement Neuroscience, UCL Queen Square Institute of Neurology, University College London (UCL), London, WC1N 3BG, UK

Corresponding author and Lead contact: james.bonaiuto@isc.cnrs.fr; @jbonaiuto

Keywords: source inversion, dipole orientation, cortical columns, cortical surface, high precision MEG

Abstract

Determining the anatomical source of brain activity non-invasively measured from EEG or MEG sensors is challenging. In order to simplify the source localization problem, many techniques introduce the assumption that current sources lie on the cortical surface. Another common assumption is that this current flow is orthogonal to the cortical surface, thereby approximating the orientation of cortical columns. However, it is not clear which cortical surface to use to define the current source locations, and normal vectors computed from a single cortical surface may not be the best approximation to the orientation of cortical columns. We compared three different surface location priors and five different approaches for estimating dipole vector orientation, both in simulations and visual and motor evoked MEG responses. We show that models with source locations on the white matter surface and using methods based on establishing correspondences between white matter and pial cortical surfaces dramatically outperform models with source locations on the pial or combined pial/white surfaces and which use methods based on the geometry of a single cortical surface in fitting evoked visual and motor responses. These methods can be easily implemented and adopted in most M/EEG analysis pipelines, with the potential to significantly improve source localization of evoked responses.

Introduction

Non-invasive measures of brain activity such as magnetoencephalography (MEG) and electroencephalography (EEG) are powerful tools for generating insights into human brain function with millisecond-scale temporal resolution. However, determining the current distribution that gives rise to the signals measured from EEG and MEG sensors is challenging (Baillet et al., 2001; Darvas et al., 2004; Fukushima et al., 2012; Haufe et al., 2011; Mattout et al., 2006). In order to simplify the source localization problem, many techniques introduce constraints to the dimensionality of source space. These constraints embody assumptions about how the brain generates the signals which we can measure from outside of the head.

One of these assumptions is that signals measured by M/EEG sensors are predominantly generated by large pyramidal neurons in deep cortical layers, which are arranged in parallel columns so that their cumulative activity produces a measurable extracranial signal (Baillet, 2017; Buzsáki et al., 2012; Murakami and Okada, 2006; Okada et al., 1997). Two commonly used source localization constraints based on this assumption are that the locations of source dipoles are restricted to locations on a mesh of the white matter surface as is it is closest to the deep cortical layers (Dale and Sereno, 1993; Henson et al., 2009; Hillebrand and Barnes, 2003, 2002; Mattout et al., 2007), and that the orientation of dipoles is orthogonal to this surface (Hämäläinen and Ilmoniemi, 1984, 1994; Henson et al., 2009; Hillebrand and Barnes, 2003; Lin et al., 2006; Salmelin et al., 1995), thereby approximating the orientation of cortical columns (Nunez and Srinivasan, 2006; Okada et al., 1997).

Using vectors orthogonal to the cortical surface may not be the best approximation to the orientation of cortical columns. Cortical folding patterns may result in curved cortical columns, and therefore their orientation with respect to the cortical surface could be different along the gray / white matter (white matter surface) and CSF / gray matter (pial surface) boundaries. Moreover, induced activity in low and high frequency bands can predominate in deep or superficial cortical layers (Bastos et al., 2015;

Bonaiuto et al., 2018a; Buffalo et al., 2011; Haegens et al., 2015; Maier et al., 2010; Spaak et al., 2012; van Kerkoerle et al., 2014), and therefore the white matter surface may not be the optimal source location model. In the past, however, the contribution of inaccuracies in dipole location and orientation constraints to source localization error has likely been insignificant in the face of within-session participant movement, co-registration error, and the relatively low resolution of cortical surface reconstructions. However, the recent development of techniques for high precision MEG (Bonaiuto et al., 2018b, 2018a; Meyer et al., 2017; Troebinger et al., 2014b, 2014a) allow us to compare competing current-flow orientation models in more detail.

Here, we set out to determine a better way to estimate the location and orientation of source dipoles based on MRI-derived cortical surfaces. We tested three different cortical surfaces for determining dipole locations: 1) white matter, 2) pial, and 3) combined white matter/pial, and five different methods for computing dipole orientations: 1) downsampled surface normals, 2) cortical patch statistics, 3) original surface normals, 4) link vectors, and 5) variational vector fields. The most commonly used method, downsampled surface normals (Dale and Sereno, 1993; Fuchs et al., 1994; Hämäläinen and Hari, 2002; Hillebrand and Barnes, 2003; Lin et al., 2006), involves downsampling (decimating) the original cortical surface, and then computing the normal vector at each vertex as the mean of the normal vectors of each surface face it is connected to. While surface decimation increases the computational tractability of source inversion, it distorts the surface faces and therefore biases the surface normal vector estimates. The cortical patch statistics method was therefore designed to compute normal vectors by averaging the individual normal vectors from vertices adjacent to the nearest vertex in the original (down-sampled) mesh (Lin et al., 2006). The original surface normals method takes advantage of the fact that the surface decimation algorithm used here maintains a correspondence between the downsampled and original surface meshes, and uses the normal vectors of the corresponding vertices from the original cortical surface. These three methods involve computation

of dipole orientation based on the geometry of a single cortical mesh: the white matter *or* pial surface. In contrast, the link vectors (Dale et al., 1999) and variational vector field (Fischl and Sereno, 2018) approaches establish correspondences between the white matter and pial surface meshes. The link vectors approach simply uses the vectors connecting each vertex on the white matter surface with the corresponding vertex on the pial surface (Dale et al., 1999). The variational vector field method constructs a field of correspondence vectors between the original white matter and pial surfaces which are constrained to be approximately normal to each cortical surface and parallel to each other (Fischl and Sereno, 2018).

We first compared the resulting orientation vectors from each method in terms of the angular difference at each surface vertex. We then ran simulations of single dipoles at a given orientation, and subsequently performed source reconstruction using various dipole orientations, noise levels, and co-registration error magnitudes. Finally, we compared the methods using evoked visual and motor responses in MEG data from human participants.

Methods

Data from eight healthy, right-handed, volunteers with normal or corrected-to-normal vision and no history of neurological or psychiatric disorders was used for our analyses (six male, aged 28.5 ± 8.52 years; Bonaiuto et al., 2018a; Little et al., 2018). The study protocol was in accordance with the Declaration of Helsinki, and all participants gave written informed consent which was approved by the UCL Research Ethics Committee (reference number 5833/001). All analysis code is available at https://github.com/jbonaiuto/dipole_orientation.

MRI acquisition

Prior to MEG scanning, two MRI scans were acquired with a 3T whole body MR system (Magnetom TIM Trio, Siemens Healthcare, Erlangen, Germany) using the body coil for radio-frequency (RF) transmission and a standard 32-channel RF head coil for reception. The first was a standard T1 for individual head-cast creation (Meyer et al., 2017), and the other was a high resolution, quantitative multiple parameter map (MPM; Weiskopf et al., 2013) for MEG source location.

The first protocol used a T1-weighted 3D spoiled fast low angle shot (FLASH) sequence with 1 mm isotropic image resolution, field-of view set to 256, 256, and 192 mm along the phase (anterior-posterior, A–P), read (head-foot, H–F), and partition (right-left, R–L) directions, respectively. The repetition time was 7.96 ms and the excitation flip angle was 12°. After each excitation, a single echo was acquired to yield a single anatomical image. A high readout bandwidth (425 Hz/pixel) was used to preserve brain morphology and no significant geometric distortions were observed in the images. Acquisition time was 3min 42s. A 12 channel head coil was used for signal reception without using either padding or headphones.

The second, MPM, protocol consisted of acquisition of three differentially-weighted, RF and gradient spoiled, multi-echo 3D fast low angle shot (FLASH) acquisitions and two additional calibration sequences to correct for inhomogeneities in the RF transmit field (Callaghan et al., 2015; Lutti et al., 2012, 2010), with whole-brain coverage at 800 µm isotropic resolution.

The FLASH acquisitions had predominantly proton density (PD), T1 or magnetization transfer saturation (MT) weighting. The flip angle was 6° for the PD- and MT-weighted volumes and 21° for the T1 weighted acquisition. MT-weighting was achieved through the application of a Gaussian RF pulse 2 kHz off resonance with 4 ms duration and a nominal flip angle of 220° prior to each excitation. The field of view was 256 mm head-foot, 224 mm anterior-posterior (AP), and 179 mm right-left (RL). Gradient echoes were acquired with alternating readout gradient polarity at eight equidistant echo times ranging from

2.34 to 18.44 ms in steps of 2.30 ms using a readout bandwidth of 488 Hz/pixel. Only six echoes were acquired for the MT-weighted acquisition in order to maintain a repetition time (TR) of 25 ms for all FLASH volumes. To accelerate the data acquisition, partially parallel imaging using the GRAPPA algorithm was employed with a speed-up factor of 2 in each phase-encoded direction (AP and RL) with forty integrated reference lines.

To maximize the accuracy of the measurements, inhomogeneity in the transmit field was mapped by acquiring spin echoes and stimulated echoes across a range of nominal flip angles following the approach described in Lutti et al. (2010), including correcting for geometric distortions of the EPI data due to B0 field inhomogeneity. Total acquisition time for all MRI scans was less than 30 min.

Quantitative maps of proton density (PD), longitudinal relaxation rate (R1 = 1/T1), MT and effective transverse relaxation rate (R2* = 1/T2*) were subsequently calculated according to the procedure described in Weiskopf et al. (2013).

FreeSurfer surface extraction

FreeSurfer (v5.3.0; Fischl, 2012) was used to extract cortical surfaces from the MPMs for MEG source localization. We used a custom FreeSurfer surface reconstruction procedure to process MPM volumes, using the PD and T1 volumes as inputs (Carey et al., 2017), resulting in surface meshes representing the pial surface (adjacent to the cerebro-spinal fluid, CSF), and the white/grey matter boundary (**Figure 1**). FreeSurfer creates the pial surface by expanding the white matter surface outward to the cortex/CSF boundary. This is done by minimizing an energy functional which includes terms promoting surface smoothness and regularity as well as an intensity-based term designed to determine the cortex/CSF boundary based on local volume intensity contrast (Dale et al., 1999). Because this process involves moving the vertices of the white matter surface based on the gradient of the energy functional, the

result is a one-to-one correspondence between white matter and pial surface vertices. We used a custom routine to downsample each of these surfaces by a factor of 10 while maintaining this correspondence. This involved using MATLAB's reducepatch function to remove vertices from, and re-tesselate the pial surface, and then removing the same vertices from the white matter surface and copying the edge structure from the pial surface. This yielded two meshes of the same size (same number of vertices and edges), comprising about 30,000 vertices each (M = 30,094.75, SD = 2,665.45 over participants).

Dipole orientation computation methods

The downsampled surface normal method computes, at each vertex of the decimated mesh, the average of the normal vectors of each adjacent face (**Figure 1**). This method was implemented using the spm_mesh_normals function in SPM12. The cortical patch statistics method computes, at each vertex of the decimated mesh, the average surface normal vector over all vertices in the original, non-decimated mesh which are adjacent to the corresponding original mesh vertex (**Figure 1**). The original surface normal method is implemented in the same way as the downsampled surface normals method, but is applied to the original, non-decimated mesh (**Figure 1**). Because our decimation procedure only removed vertices from the original surface, the resulting vectors can then be mapped onto the vertices of the decimated mesh used for source localization. The link vectors method takes advantage of the fact that our decimation routine maintains the correspondence between white matter and pial surface vertices, and for each vertex on the pial surface, uses the vector linking it to the corresponding vertex on the white matter surface ($\mathbf{v}_i=\mathbf{w}_i - \mathbf{p}_i$, for the i^{th} white matter vertex, w_i, and pial vertex p_i; **Figure 1**). The variational vector field method constructs a vector field linking the white matter and pial surfaces, by using gradient descent to minimize an energy functional that encourages vectors to approximate surface

normals and to be parallel to each other (Fischl and Sereno, 2018) (**Figure 1**). The angular difference between any two vectors, v_1 and v_2, was computed using the formula: atan2(||$\mathbf{v_1} \times \mathbf{v_2}$||, $\mathbf{v_1} \cdot \mathbf{v_2}$).

Vectors obtained from each method were used to construct the lead field matrix of the forward model used for source inversion of the simulated or experimental data. The models constructed using each method were compared to each other based on relative Bayesian model evidence, as approximated by differences in free energy:

$$\Delta F_{i,j} = F_i - F_j$$

where F_i and F_j are the free energy values of models *i* and *j*, respectively. Free energy is a parametric metric rewards fit accuracy and penalizes model complexity (Bonaiuto et al., 2018b; Friston et al., 2008, 2007; Henson et al., 2009; López et al., 2014; Wipf and Nagarajan, 2009):

$$F_i = \text{Accuracy}(i) - \text{Complexity}(i)$$

The first term is the log model evidence: the log of the probability of the data, given the model and parameters, and the second term is the Kullback-Liebler divergence between the true posterior density and an approximate posterior density. Because the second term is always positive, free energy provides a lower bound on the model evidence (Penny et al., 2010).

The best overall dipole orientation method and source space surface model was determined using random effects family level Bayesian inference (Penny et al., 2010) as implemented by the spm_compare_families method in SPM12. This method groups models based on visual ERF 1 and 2 and the motor ERF in all participants into 'families', and then combines the evidence of models from the same family and computes the exceedance probability for each family. The exceedance probability corresponds to the belief that a particular model family is more likely than the other model families tested, given the data from all participants. We first grouped models into families based on dipole orientation method / source space surface model combinations (e.g. downsampled surface normals /

pial surface) to determine the best combination over all ERFs and participants. We then grouped models based on dipole orientation method, and finally based on source space surface model.

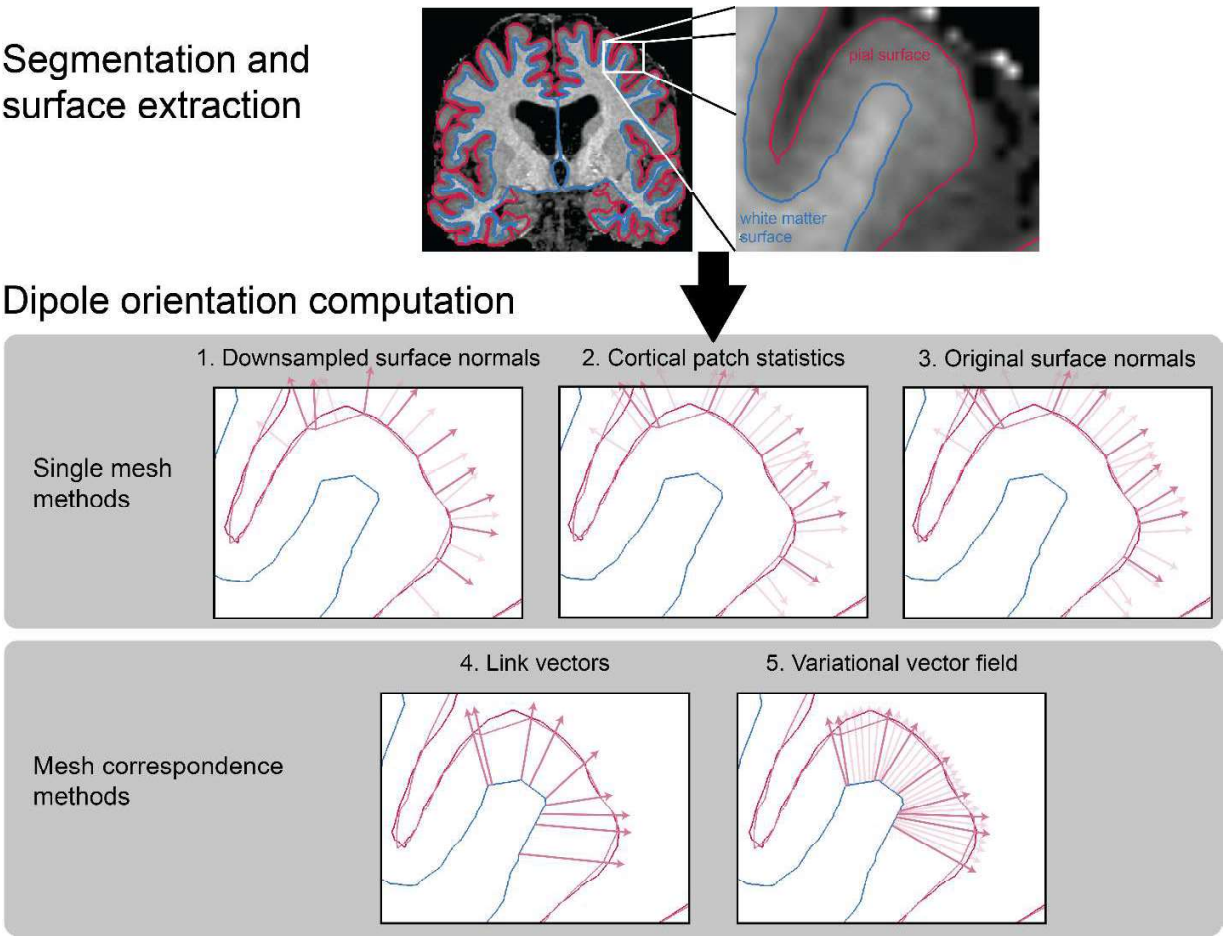

Figure 1. Dipole orientation models.
Pial and white matter surfaces are extracted from proton density and T1 weighted quantitative maps obtained from a multi-parameter mapping MRI protocol. Dipole orientation vectors are computed from these surfaces using five different methods. The downsampled surface normal and original surface normal methods compute vectors at each vertex (dark red) as the mean of the normal vectors of the surface faces they are connected to (light red). The cortical patch statistics method computes the mean of the normal vertices adjacent to the corresponding vertices in the original mesh. The link vectors method computes vectors which link corresponding vertices on the white matter and pial surfaces. The variational vector field method constructs a field of vectors which are approximately parallel to each other and orthogonal to the pial surface (shown in light red for the original surfaces and dark red for the subset of vertices in the downsampled surfaces).

Simulations

All simulations were based on a single dataset acquired from one human participant. This dataset was only used to determine the sensor layout, sampling rate (1200 Hz, downsampled to 250 Hz), number of trials (515), and number of samples (251) for the simulations. All simulations and analyses were implemented using the SPM12 software package (http://www.fil.ion.ucl.ac.uk/spm/software/spm12/).

In each simulation, we specified spatially distributed source activity centered at a single vertex on the pial surface. We simulated a Gaussian activity time course in this vertex, centered within the epoch, with a width of 25ms and a magnitude of 10nAm. We then spatially smoothed this simulated dipole time course with a Gaussian kernel (FWHM=5mm), to obtain a patch of spatially distributed activity. Within this patch, the orientation of each vertex differed, but was specified by the same rule using the link vectors method. We then used a single shell forward model (Nolte, 2003) to generate a synthetic dataset from the simulated source activity. We simulated sources at 100 random vertices on the pial surface, and ran two sets of simulations: one varying the level of noise in the simulated data and the other varying the magnitude of co-registration error.

Typical per-trial SNR levels for MEG data range from −40 to −20 dB (Goldenholz et al., 2009), and therefore Gaussian white noise was added to the simulated data and scaled in order to yield per-trial amplitude SNR levels (averaged over all sensors) of −50, -40, -30, −20, -10, or 0 dB to generate synthetic datasets across a range of realistic SNRs. Source reconstruction was performed using 10 different models. The reference model used the original link vectors as dipole orientation priors, and the remaining 9 models used vectors with angular differences from the original link vectors ranging from 7 to 63 degrees (in increments of 7 degrees). The orientation of the 9 additional vectors was determined by taking random points on the edge of a cone defined by the reference vector and the angular distance. In these simulations, the co-registration error was 0mm. Within each SNR level, the free energy metric was compared between each model and the reference model.

Within-session head movement and between-session co-registration error commonly combine to introduce a typical magnitude of ~5mm (or more) of uncertainty concerning the relative location of the brain and the MEG sensors in traditional MEG recordings (Adjamian et al., 2004; Gross et al., 2013; Ross et al., 2011; Singh et al., 1997; Stolk et al., 2013; Whalen et al., 2008). To simulate between-session co-registration error, we therefore introduced a linear transformation of the fiducial coil locations in random directions (0mm translation - 0° rotation, 2mm - 2°, 4mm - 4°, 6mm - 6°, 8mm - 8°, or 10mm - 10°) prior to source inversion. As in the SNR simulations, source reconstruction was performed using a reference model with the original link vectors as orientation priors, and 9 models using vectors rotated in random directions with angular differences from the original vectors from 7 to 63 degrees. In these simulations, the per-trial amplitude SNR was set to 0dB. Within each level of co-registration error, we compared the free energy between each model and the reference model.

Head-cast construction

From an MRI-extracted image of the scalp, a head-cast that fit between the participant's scalp and the MEG dewar was constructed (Bonaiuto et al., 2018a; Meyer et al., 2017; Troebinger et al., 2014b). Scalp surfaces were first extracted from the T1-weighted MRI scans acquired in the first MRI protocol using SPM12 (http://www.fil.ion.ucl.ac.uk/spm/). This tessellated surface, along with 3D models of fiducial coils placed on the nasion and the left and right pre-auricular points, was used to create a virtual 3D model, which was then placed inside a virtual version of the scanner dewar in order to minimize the distance to the sensors while ensuring that the participant's vision was not obstructed. The model (including spacing elements and ficudial coil protrusions) was printed using a Zcorp 3D printer (Zprinter 510). The 3D printed model was then placed inside a replica of the MEG dewar and polyurethane foam was poured in between the surfaces to create the participant-specific head-cast. The protrusions in the 3D model for fiducial coils therefore become indentations in the foam head-cast, into which the fiducial

coils can be placed scanning. The locations of anatomical landmarks used for co-registration are thus unchanged over repeated scans, allowing combination of data from multiple sessions (Bonaiuto et al., 2018a; Meyer et al., 2017).

Behavioral task

Participants completed a visually cued action decision making task in which they responded to visual instruction cue projected on a screen by pressing one of two buttons using the index and middle finger of their right hand (Bonaiuto et al., 2018a). After a baseline period of fixation, a random dot kinematogram (RDK) was displayed for 2s with coherent motion either to the left or to the right. Following a delay period, an instruction cue (an arrow pointing either to the left or the right), prompted participants to press either the left or right button. The level of motion coherence in the RDK and the congruence between the RDK motion direction and instruction cue varied from trial to trial, but for the purposes of the present study, we analyzed the main effect of visual stimulus onset and button press responses. For a full description of the paradigm and task structure, see Bonaiuto et al. (2018a).

Each block contained 180 trials in total. Participants completed three blocks per session, and 1–5 sessions on different days, resulting in 540–2700 trials per participant (M = 1822.5, SD = 813.21). The task was implemented in MATLAB (The MathWorks, Inc., Natick, MA) using the Cogent 2000 toolbox (http://www.vislab.ucl.ac.uk/cogent.php).

MEG acquisition and preprocessing

MEG data were acquired using a 275-channel Canadian Thin Films (CTF) MEG system with superconducting quantum interference device (SQUID)-based axial gradiometers (VSM MedTech, Vancouver, Canada) in a magnetically shielded room. A projector was used to display visual stimuli on a

screen (~50 cm from the participant), and a button box was used for participant responses. The data collected were digitized continuously at a sampling rate of 1200 Hz. MEG data preprocessing and analyses were performed using SPM12 (http://www.fil.ion.ucl.ac.uk/spm/) using MATLAB R2014a. The data were filtered (5th order Butterworth bandpass filter: 2–100 Hz, Notch filter: 50 Hz) and downsampled to 250Hz. Eye blink artifacts were removed using multiple source eye correction (Berg and Scherg, 1994). Trials were then epoched from 1s before RDK onset to 1.5s after instruction cue onset for analysis of visual responses, and from 2s before the participant's response to 2s after for analysis of movement-evoked responses. Blocks within each session were merged, and trials whose variance exceeded 2.5 standard deviations from the mean were excluded from analysis. The epoched data were then averaged over trials using robust averaging, a form of general linear modeling (Wager et al., 2005) used to reduce the influence of outliers on the mean by iteratively computing a weighting factor for each sample according to how far it is from the mean. Preprocessing code is available at http://github.com/jbonaiuto/meg-laminar.

Source reconstruction

Source inversion was performed using the empirical Bayesian beamformer algorithm (EBB; Belardinelli et al., 2012; López et al., 2014) as implemented in SPM12. The source inversion was applied to a 100ms time window, centered on the event of interest (the peak of the simulated signal, 100ms following the onset of visual stimuli, or the button press response). These data were projected into 274 orthogonal spatial (lead field) modes and 4 temporal modes. Singular value decomposition (SVD) was used to reduce the sensor data to 274 orthogonal spatial (lead field) modes, each with 4 temporal modes (weighting the dominant modes of temporal variation across the window). For uninformative priors, the maximum-likelihood solution to the inverse problem is:

$$\hat{J} = QL^T(Q_\epsilon + LQL^T)^{-1}Y$$

where $\hat{J}$ is the estimated current density across the source space, Y is the SVD-reduced measured data, L is the lead field matrix that can be computed from the sensor and volume conductor geometry. Q_ϵ is the sensor covariance and Q is the prior estimate of source covariance. We assumed the sensor level covariance (Q_ϵ) to be an identity matrix (see discussion). Most inversion algorithms can be differentiated by the form of Q (Friston et al., 2008; López et al., 2014). EBB uses a beamformer prior to estimate the structure of Q (Belardinelli et al., 2012; López et al., 2014) based on the sensor-level data:

$$\mathrm{Q}(i) = \frac{1}{L_i^T L_i}\left(L_i^T (YY^T)^{-1} L_i + \lambda I\right)^{-1}$$

where each element of the diagonal $Q(i)$ corresponds to a source location i. The lead field of each source location is L_i, ^{T} denotes the transpose operator, I is an identity matrix, and λ is a regularization constant (set to 0). The prior estimates of Q_ϵ and Q are then re-scaled or optimally mixed using an expectation maximization scheme (Friston et al., 2008) to give an estimate of J that maximizes model evidence. All inversions used a spatial coherence prior (Friston et al., 2008) with a FWHM of 5 mm. We used the Nolte single shell head model (Nolte, 2003).

For MEG source inversion, the accuracy term of the free energy equation is defined as

$$\mathrm{Accuracy}(i) = \frac{N_c}{2}\mathrm{trace}\left(C_Y C_i^{-1}\right) - \frac{N_c}{2}\log|C_i| - \frac{N_c N_t}{2}\log(2\pi)$$

where N_c is the number of channels, N_t is the number of samples, $C_Y = \frac{1}{N_c}YY^T$ is the data-based sampled covariance, $C_i = Q_\epsilon + L_i Q L_i^T N_t$ is the model-based sample covariance, and $|\cdot|$ is the matrix determinant operator.

For the EBB algorithm, the complexity term of the free energy equation is dependent on hyperparameters, λ, that control the trade-off between sensor noise $Q_\epsilon = \lambda_1 I_{N_c}$, and the beamforming prior $Q = \lambda_2 \Gamma$, where Γ is the beamforming prior:

$$\text{Complexity}(i) = \frac{1}{2}\left(\hat{\lambda}_i - \upsilon\right)^T \Pi\left(\hat{\lambda}_i - \upsilon\right) + \frac{1}{2}\log\left|\Sigma_{\lambda_i}\Pi\right|$$

The prior and posterior distributions of λ, $q(\lambda_i)$ and $p(\lambda_i)$ are assumed to be Gaussian:

$$q(\lambda_i) = N(\lambda; \upsilon, \Pi^{-1})$$

$$p(\lambda_i) = N(\hat{\lambda}_i, \Sigma_{\lambda_i})$$

where $\hat{\lambda}_i$ and Σ_{λ_i} are the posterior mean and covariance of the hyperparameters for model *i*. We used non-informative mean and precision (υ and Π) implemented as identity matrices scaled close to zero mean and low precision, as implemented by default in SPM.

Results

Different methods for estimating vector orientation yield substantial variation in dipole orientation

We first compared the dipole orientation vectors generated by each of our five methods in terms of the angular difference between vectors at the same vertex on the pial and white matter surfaces, respectively (**Figure 2**). The three methods that utilize only one surface, (downsampled surface normals, cortical patch statistics, original surface normals) generated vectors which were the most similar to each other on both the pial (downsampled surface normals – cortical patch statistics individual subject mean angular difference: 19.16-23.04°; over subjects: M=22.30°, SD=1.51°; downsampled surface normals – original surface normals: 16.00-17.95°; over subjects: M=16.94°, SD=0.67°; cortical patch statistics – original surface normals: 17.80-22.89°; over subjects: M=21.01°, SD=1.55°) and white matter surfaces (downsampled surface normals – cortical patch statistics individual subject mean angular difference:

346 10.65-11.35°; over subjects: M=10.99°, SD=0.27°; downsampled surface normals – original surface
347 normals: 9.64-10.57°; over subjects: M=10.10°, SD=0.32°; cortical patch statistics – original surface
348 normals: 8.93-9.76°; over subjects: M=9.34°, SD=0.31°). Each single- and multi-surface method
349 generated vectors with mean angular differences from each other of at least 20°, for both the pial
350 surface (downsampled surface normals – link vectors: 22.94-29.56°, M=24.51°, SD=2.15°; downsampled
351 surface normals – variational vector field: 25.52-27.13°, M=26.05°, SD=0.55°; cortical patch statistics –
352 link vectors: 25.26-32.76°, M=27.42°, SD=2.06°; cortical patch statistics – variational vector field: 28.80-
353 32.55°, M=30.91°, SD=1.11°; original surface normals – link vectors: 26.77-33.12°, M=28.44°, SD=2.06°;
354 original surface normals – variational vector field: 26.18-28.43°, M=27.06°, SD=0.75°) and the white
355 matter surface (downsampled surface normals – link vectors: 21.81-29.03°, M=23.46°, SD=2.33°;
356 downsampled surface normals – variational vector field: 27.08-36.26°, M=28.78°, SD=3.06°; cortical
357 patch statistics – link vectors: 22.64-24.82°, M=24.48°, SD=2.34°; cortical patch statistics – variational
358 vector field: 27.31-36.34°, M=29.04°, SD=3.00°; original surface normals – link vectors: 23.38-30.09°,
359 M=25.00°, SD=2.15°; original surface normals – variational vector field: 26.43-35.69°, M=28.31°,
360 SD=3.08°). The two multi-surface methods, link vectors and variational vector field, generated vectors
361 with some of the largest mean angular differences of all method pairs on each surface (pial surface:
362 67.41-30.74°, M=27.71°, SD=1.40°; white matter surface: 31.33-40.74°, M=33.31°, SD=3.04°). These
363 results were comparable when using surfaces derived from more commonly used $1mm^3$ T1 scans
364 instead of $800\mu m^3$ MPMs (**Figure S1**). Therefore, rather than being close approximations to each other,
365 each method generates substantially different dipole orientation vectors, even within the multi-surface
366 class of methods.

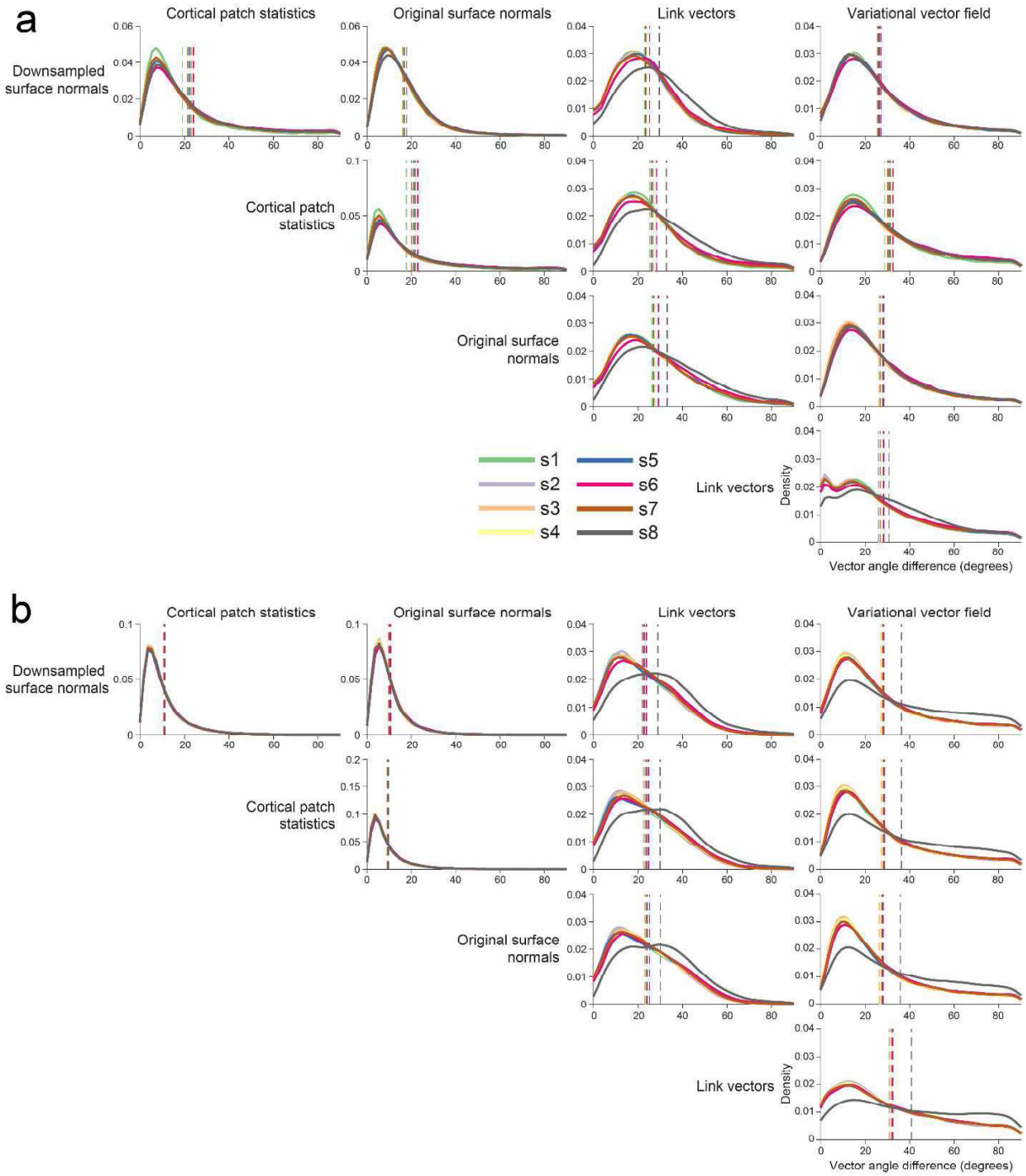

Figure 2. Substantial discrepancy in dipole orientations across methods.
*Distribution of angular difference between dipole orientations on the pial surface (**a**) and white matter surface (**b**), generated using each method for each participant. Vertical dashed lines show the mean angular difference for each participant.*

We next compared dipole orientation vectors generated by each method between the pial and white matter surfaces derived from the 800µm^3 MPM volumes (**Figure 3**) and 1mm^3 T1 volumes (**Figure S2**). Because the link vectors method generates vectors that connect corresponding vertices on the pial and white matter surfaces, the resulting dipole orientations on each surface are equivalent (i.e. the link vector from a particular vertex on the pial surface points in exactly the opposite direction as the link vector from the corresponding white matter surface vertex). All three single-surface methods generated vectors with the lowest average angular difference between pial and white matter surfaces created using either the 800µm^3 MPM volumes (downsampled surface normals: individual subject mean angular difference=16.88-20.52°, over subjects M=18.23°, SD=1.13°; cortical patch statistics: 22.66-27.81°, M=25.70°, SD=1.67°; original surface normals: 22.90-26.81°, M=24.46°, SD=1.26°) or the 1mm^3 T1 volumes (downsampled surface normals: 17.89-19.49°, M=18.66°, SD=0.56°; cortical patch statistics: 25.10-27.23°, M=26.23°, SD=0.70°; original surface normals: 24.10-28.80°, M=25.45°, SD=1.46°). The variational vector field method generated dipole orientation vectors that differed the most between the pial and white matter surface (MPM: 37.47-43.54°, M=38.80°, SD=1.99°; T1: 37.07-40.28°, M=39.10°, SD=1.00°). Aside from the link vectors method, there is therefore at least as much variation in dipole orientations between the pial and white matter surfaces within a method as there is between methods for one surface.

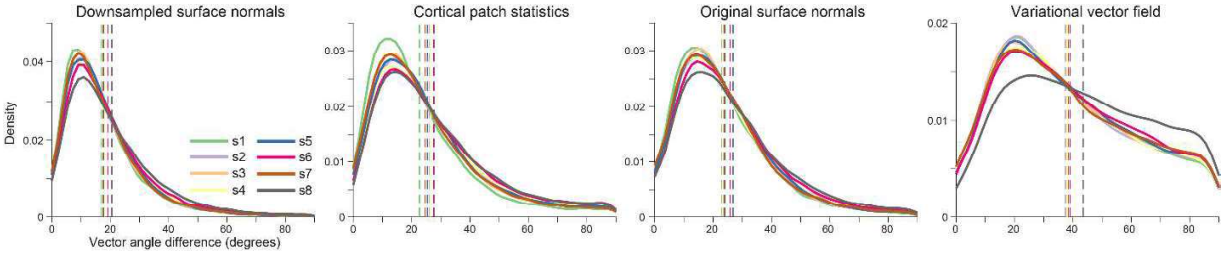

Figure 3. Substantial discrepancy in dipole orientations between pial and white matter surfaces. *Distribution of angular difference between dipole orientations at corresponding vertices on the pial and white matter surfaces, generated using the 800 µm^3 MPM volumes. The link vectors method is not shown because this method generates identical dipole orientations for the pial and white matter surfaces. Each solid line shows the distribution for a single participant. Vertical dashed lines show the mean angular difference for each participant.*

With high precision MEG data, getting the orientation right matters

Having established that each method yields substantially different orientation vectors, we next sought to determine the minimum angular difference between dipole orientations distinguishable by source inversion model comparison, and how this is affected by typical levels of SNR and co-registration error. We therefore simulated dipoles at 100 random source locations on the pial surface and created synthetic datasets with varying SNR and co-registration error levels. We then performed source inversion on the synthetic datasets, using a reference model in which the dipole orientations exactly match those of the simulated dipole, and 9 other models in which the dipole orientations were rotated with respect to simulated dipole orientation. We then compared each of these models to the reference model in terms of the relative free energy, using a significance threshold of ±3 for the free energy difference (indicating that one model is approximately twenty times more likely than the other).

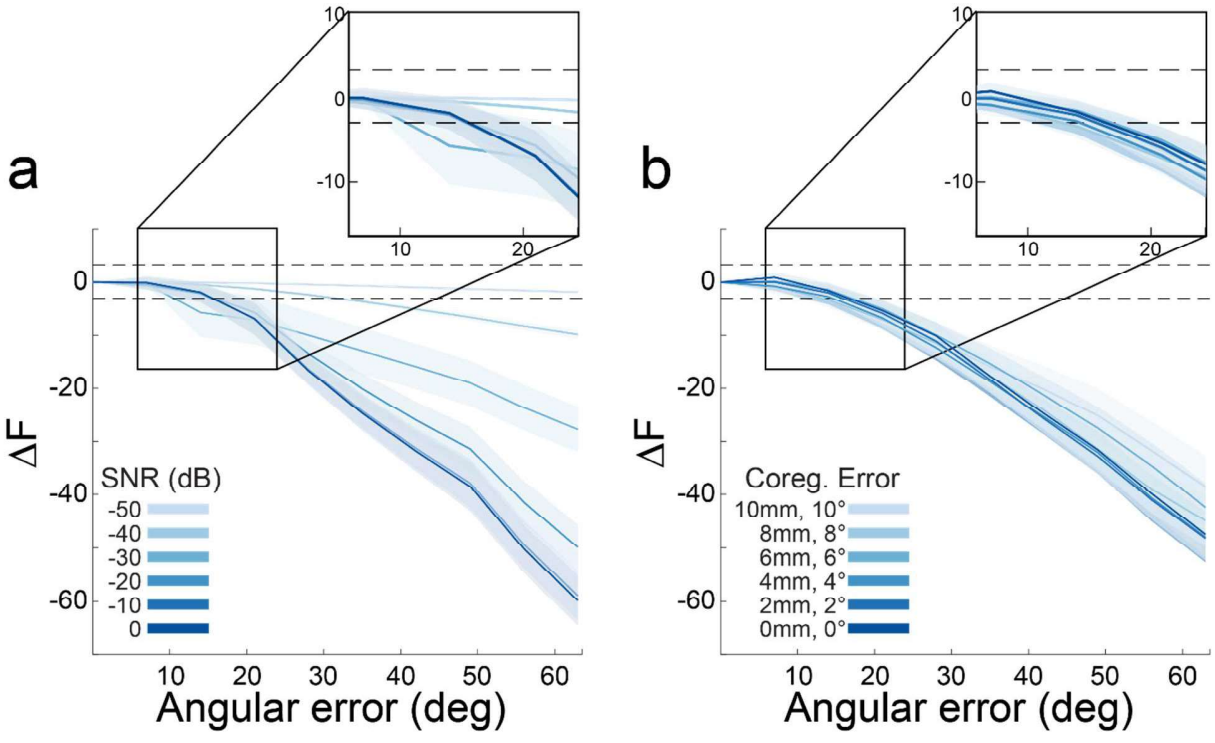

Figure 4. With high precision MEG data, model evidence decreases with dipole orientation error.
a *Each line shows the change in model evidence (ΔF) as the orientation of the dipole used for inversion is rotated away from the true orientation at different SNR levels (co-registration error=0mm). The shaded regions represent the standard error of ΔF over*

all 100 simulations at each angular error value tested. The lower dotted line (at ΔF=-3) show the point at which the imperfect model is 20 times less likely than the true model. The differences between models become more apparent at higher SNR.
b *As in a, for different magnitudes of co-registration error (SNR=0dB). Co-registration error has a smaller impact than SNR on discriminating between models with different dipole orientations.*

At lower SNR levels (-50dB), each model was indistinguishable from the reference model (magnitude of relative free energy less than 3). However, as SNR increased, models with an angular error as low as 15 degrees relative to the reference model started to become differentiable (i.e., a relative free energy difference of >3; **Figure 4a**). Relative model evidence was less dependent on co-registration error, and at all levels tested models with an angular error of at least 15 degrees could be differentiated from the reference model (**Figure 4b**). This angular error is well within the range of the angular differences between vectors generated by each of the methods considered here (**Figure 2**). In other words, given sufficient SNR and co-registration accuracy, one should be able to determine the best method to use with human data based on source inversion model comparison.

Comparing surface models with empirical head-cast data

We next compared orientation models based on three different evoked responses from human participants. We performed source inversion, and compared the resulting model fits in terms of relative free energy compared to that of the downsampled surface normal model (the current most commonly used method). This was repeated using source space models restricted to the pial surface, white matter surface, and combined pial – white matter surface (Bonaiuto et al., 2018a, 2018b). In this case the combined pial-white model had double the number of sources and these sources could be arranged with identical orientations on each surface (link vectors); or different orientations (cortical patch statistics, downsampled surface normals, original surface normals, and variational vector field).

435 The evoked response fields (ERFs) were the visually-evoked response to the RDK (visual ERF 1) and
436 instruction cue (visual ERF 2), and the motor-evoked response during the button press (motor ERF).
437 When running the source inversion over the full time course of each ERF, each orientation model
438 yielded slightly different peak cortical locations (**Figure 5**a, b), with the original surface normals and
439 variational vector field methods giving the closest peak coordinates (M=4.88mm, SD=2.93mm), and the
440 cortical patch statistics and link vectors methods yielding coordinates furthest away from each other
441 (M=13.96mm, SD=12.76mm). At each peak location identified by the downsampled surface normals
442 method, the source space ERFs given by the downsampled surface normals, cortical patch statistics, and
443 variational vector field methods, respectively, were most similar to each other, whilst the link vectors
444 methods yielded an ERF with a larger amplitude, and the original surface normals method yielded an
445 ERF with inverted polarity (RMSE<0.1; **Figure 5**c, d). However, at the peak coordinate identified by each
446 method the ERFs were very similar (RMSE<0.05; **Figure 5**e, f).

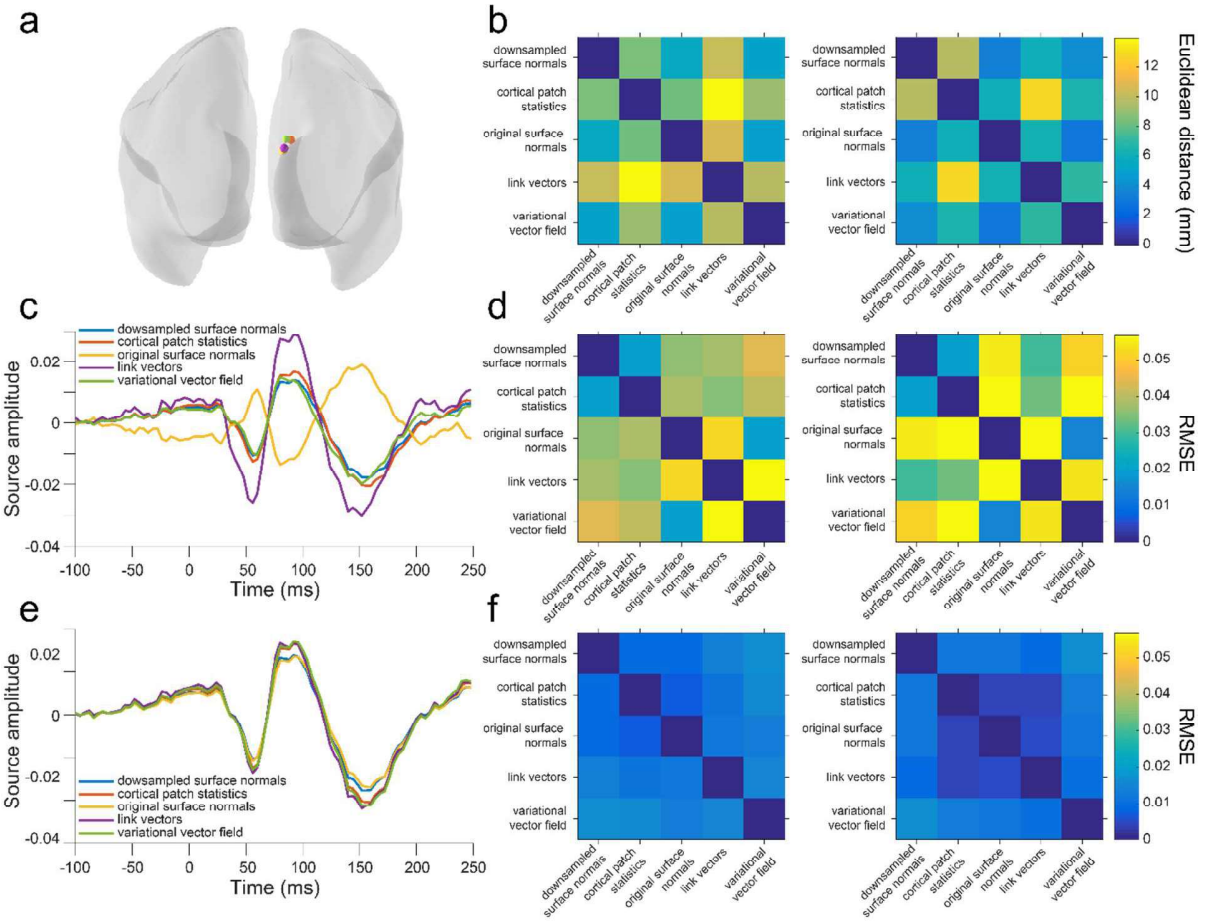

Figure 5: Variation in source localization across methods.
a *Peak source locations on the pial surface for visual ERF1, for each dipole orientation method, in a single subject.*
b *Mean (left) and standard deviation (right) of the Euclidean distance between peak source locations for each method, using the pial surface, over subjects and ERFs.*
c *Time course of source activity for visual ERF1 for the different methods, at the peak pial source location identified using the downsampled surface normals method, for a single subject.*
d *Mean (left) and standard deviation (right) of the RMSE between source activity time courses at the peak source location identified using the downsampled surface normals method, for each method, using the pial surface, over subjects and ERFs.*
e *Time course of source activity for visual ERF1 at the peak pial source location identified from each method, for a single subject.*
f *Mean (left) and standard deviation (right) of the RMSE between source activity time courses at the peak source location identified using each method with the pial surface, over subjects and ERFs.*

We then compared each method in terms of model fit. The link vectors method achieved a significantly better model fit than the downsampled surface normal method in 7/8 subjects for visual ERF 1 and 2 and the motor ERF using the pial surface, 7/8 subjects for visual ERF 1 and the motor ERF and 8/8 subjects for visual ERF 2 using the white matter surface, and 7/8 subjects for visual ERF 1 and 2 and the motor ERF using the two-layer surface (**Figure 6b**). The variational vector field method had significantly better model fit than the downsampled surface normal method in 6/8 subjects for visual ERF 1 and 4/8

subjects for visual ERF2, but only 2/8 subjects for the motor ERF using the pial surface, 1/8 subjects for visual ERF 1 and the motor ERF and 4/8 subjects for visual ERF 2 using the white matter surface, and 5/8 subjects for visual ERF 1 and 2 and 1/8 subjects for the motor ERF using the two-layer surface. The original surface normal method was most similar to the downsampled surface normal method, only being significantly better in 4/8 subjects for visual ERF1, 5/8 subjects for visual ERF2, and 0/8 subjects for the motor ERF using the pial surface, 0/8 subjects for visual ERF 1 and 2 and the motor ERF using the white matter surface, and 1/8 subjects for visual ERF 1, 3/8 subjects for visual ERF2, and 0/8 subjects for the motor ERF using the two-layer surface. The cortical patch statistics method was significantly better than the downsampled surface normals method in 3/8 subjects for visual ERF 1, 6/8 subjects for visual ERF 2, and 2/8 subjects for the motor ERF using the pial surface, 0/8 subjects for visual ERF 1 and 2 and the motor ERF using the white matter surface, and 2/8 subjects for visual ERF 1, 4/8 subjects for visual ERF 2, and 0/8 subjects for the motor ERF.

While the cortical patch statistics and original surface normal methods are an improvement on the widely used downsampled surface normal method, multi-surface methods such as link vectors and variational vector fields achieve better model fits overall, using either single- or two-layer cortical surface models (**Figure 6b**). These results were comparable when using surfaces derived from more commonly used $1mm^3$ T1 scans instead of $800\mu m^3$ MPMs, with the exception of the variational vector field method, which performed significantly worse than the downsampled surface normal method in 6/8 subjects for the motor ERF using the pial surface (**Figure S3**).

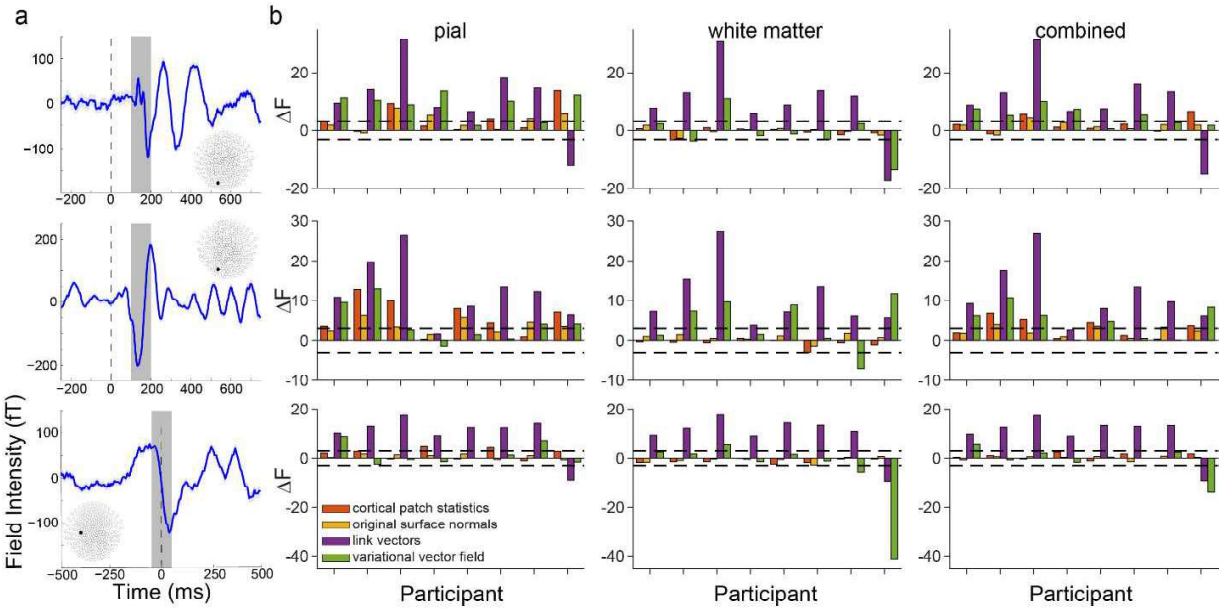

Figure 6. Surface correspondence-based methods yield the best model fit.
a *Trial-averaged event-related fields (ERFs) aligned to the onset of visual stimulus 1 (the random dot kinematogram; top), visual stimulus 2 (the instruction cue; middle), and to the participant's response (button press; bottom). Data shown are for a single representative participant. The inlays show the MEG sensor layout with filled circles denoting the sensor from which the ERFs are recorded. Each shaded region represents the time window over which source inversion was performed.*
b *Change in free energy (relative to the downsampled surface normals model) for each method tested for each participant for visual ERF 1 (top), visual ERF 2 (middle), and the motor ERF (bottom) using vectors derived from 800µm^3 MPM volumes and source space models based on the pial (left), white matter (center), and combined pial / white matter surfaces (right).*

Interaction between orientation and source space models

We next sought to establish how the orientation models interacted with the different possible choices of source space, specifically the cortical surface used to define source locations and the surface used to compute dipole orientations. We fit the empirical evoked response data, using source space location models based on the white matter, pial, or combined white matter/pial surfaces, and for each orientation model using the white matter, pial, or combined white matter/pial surfaces (with the exception of the combined surface source space orientation model which can only be used with the combined surface source space location model).

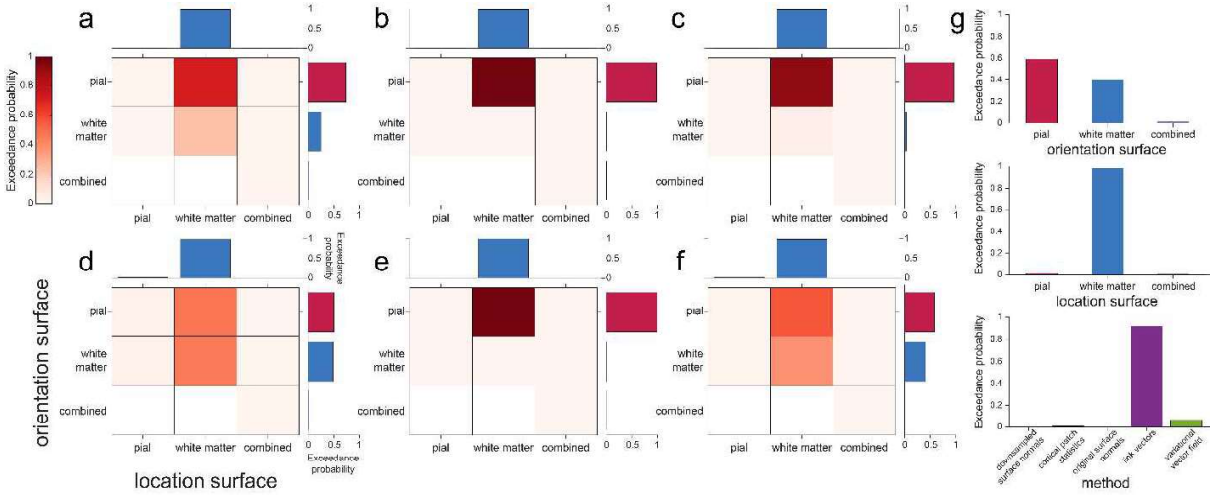

Figure 7. Source inversion using the pial surface and surface correspondence-based methods yield the best model fit overall.
a-e *Exceedance probabilities for each combination of source space orientation (pial, white matter, and combined) and location (pial, white matter, and combined) models for each dipole orientation vector method tested (**a** downsampled surface normals, **b** cortical patch statistics, **c** original surface normals, **d** link vectors, **e** variational vector field) using surfaces derived from 800μm^3 MPM volumes. In each panel the top and right plots show exceedance probabilities for models grouped by source space location or orientation model alone.*
f *As in **a-e**, for each source space orientation and location models over all dipole orientation vector methods.*
g *Exceedance probabilities for each source space orientation model over all source space location models and dipole orientation vector methods (top), for each source space location model over all source space orientation models and dipole orientation vector methods (middle), and for each dipole orientation vector method over all source space orientation and location models (bottom).*

To compare source space surface location and orientation models, we used random effects family level Bayesian inference (Penny et al., 2010) over the results from visual ERF 1 and 2 and the motor ERF in all participants. This method groups models into 'families', and then combines the evidence of models from the same family to compute the exceedance probability (EP) for each model family. This corresponds to the belief that a particular model family is more likely than the other model families tested, given the data from all participants. We first compared combinations of source space location and orientation surface models within each method, and found that for most dipole orientation methods (downsampled surface normals, cortical patch statistics, original surface normals, and variational vector field), the best source orientation space model was the pial surface and the best source space location model was the white matter surface (downsampled surface normals EP = 0.708, cortical patch statistics EP = 0.968, original surface normals EP = 0.924, variational vector field EP = 0.975; **Figure 7a-c**,**e**). For the link

vectors method, the best source space location model was the white matter surface, and the pial and white matter source space orientation models were nearly indistinguishable (pial orientation model EP = 0.458, white matter orientation model EP = 0.468; **Figure 7d**). This was not unexpected because the orientation vectors generated from these surfaces using the link vectors method are exactly 180° to each other. Over all dipole orientation methods, the best source space orientation surface was the pial surface and the best source space location model was the white matter surface (EP = 0.654; **Figure 7f**). We then grouped models into families based on the source space surface used for orientation and location. This confirmed that the models using the pial surface to compute dipole orientation provided the best model fit, with an EP of 0.608 (white matter surface EP = 0.379), and models using the white matter surface to define source space locations outperformed the others, with an EP of 0.985 (**Figure 7g**). Finally, we grouped models based on the method used to compute dipole orientation vectors and confirmed that the link vectors and variational vector field methods were the best overall, with EPs of 0.918 and 0.064, respectively (**Figure 7g**). Using surfaces obtained from $1mm^3$ T1 volumes yielded the same results (**Figure S4**).

Discussion

In this paper we show that methods for computing dipole orientation which are based on establishing correspondences between white matter and pial cortical surfaces dramatically outperform methods based on the geometry of a single cortical surface in fitting evoked visual and motor responses. To this end, we compared five different approaches for estimating dipole vector orientation, both in simulations and visual and motor evoked MEG responses.

Our results show substantial variation in dipole vector orientation across the different methods. This indicates that the choice of method is likely to significantly impact the quality of source estimation. At low SNR levels and with head movements commonly observed in conventional MEG recordings, this influence is small or non-detectable. However, with the increased SNR and reduced head movements afforded by high-precision MEG (Meyer et al., 2017; Troebinger et al., 2014b), these differences become distinguishable when average angular errors between methods vary by around 15 degrees. These small orientation errors put a hard limit on any possible improvements in non-invasive estimates of cortical current flow. For example Hillebrand & Barnes (2003) showed that small orientation errors resulted in localization errors which increased monotonically with SNR.

This means that with higher precision MEG recordings, accurate estimation of the dipole orientation becomes increasingly important. Consequently, conventional approaches which estimate vector orientation from a single (downsampled) surface, and based on lower resolution MRI volumes, are likely to offer limited accuracy in source estimation, at least for evoked fields, as analyzed here. By contrast, methods that utilize link vectors between pial and white matter surfaces constructed from higher resolution structural images perform significantly better in explaining observed evoked responses.

The average angular differences between the five methods compared here were substantial, with means of 18-30 degrees, both in high-resolution MPMs and in commonly used T1-weighted structural

images with $1mm^3$ spatial resolution. We do not know the ground truth of current flow orientation in the brain, but we show here that the average angular difference between methods is within the range distinguishable in simulated data with SNR and co-registration error levels achievable with high precision MEG. We were therefore able to compare these methods in terms of how well they fit human MEG data, leveraging the free energy metric, in order to determine which method best estimates true dipole orientations.

We were surprised by the large variation in orientation estimates from the same anatomy using different methods. The typical expected orientation differences between methods was ~20-30 degrees. This in turn led to differences in estimated source location of ~5-14mm. In this study we sought to minimize head-movement and co-registration errors by using head-casts, but in typical MEG studies such additional errors will only add to this variation. Based on these estimates it would seem that if precise anatomical information (e.g. from high resolution MRI volumes) is not available then an approach using some form of loose orientation constraint is advisable (Lin et al., 2006). However, one advantage of being able to exploit anatomical information is to use the sensitivity of MEG to cortical orientation to refine the source localization.

While the family of source space location models based on the white matter surface yielded the highest exceedance probability, the results of the surface comparison varied by evoked response and dipole orientation computation method. Evoked responses can be broken down into temporally dynamic components and therefore may be the result of a complex temporal pattern of signals in both deep and superficial cortical layers. We here used the same 100ms time window for source inversion in all participants and therefore this analysis did not take into account between-participant differences in the timing of evoked responses and could not track the time course of laminar activity. The inherent differences between induced and evoked responses may therefore explain the more variable attribution of the evoked response to pial and white matters surfaces, compared to the bias of high- and low

590 frequency signals towards deep and superficial cortical laminae, respectively (Bonaiuto et al., 2018a).
591 Future extensions of this work could utilize source inversion in successive time bins to address this
592 limitation and generate temporally resolved estimates of laminar activity.

593 We assumed the sensor level covariance matrix to be diagonal. However, an independent sensor
594 dataset recorded during a similar time period in an empty room, showed off-diagonal structure (**Figure**
595 **S5**). Importantly, the same pattern of model comparison results was obtained when using a sensor
596 covariance matrix based on these noise measurements (**Figure S6, S7**).

597 In this work, we used free energy as our metric of model fit but we would expect these findings to
598 generalize across other metrics. For example, we have previously shown that for model comparison
599 problems of the type utilized in this study, free energy is very highly correlated with nonparametric cross
600 validation error measures of model fit (Bonaiuto et al., 2018b).

601 The present findings do not just impact high SNR MEG recordings obtained with cryogenic sensors, but
602 also for new generations of cryogen-free MEG sensors (optically-pumped magnetometers; OPMs). These
603 sensors can be worn on the head and permit long-duration recordings without head-to-sensor
604 movement, with accurate knowledge of each sensor's position with respect to the brain (Boto et al.,
605 2018, 2017; Holmes et al., 2018; Iivanainen et al., 2019, 2017; Knappe et al., 2014). Our results show
606 that source estimation for this type of recordings is likely to benefit from methods that estimate vector
607 orientation based on white matter – pial surface vertex correspondences, as opposed to more
608 commonly used techniques employing a single surface.

609 We here assumed that straight vectors provide the best approximation of the orientation of cortical
610 columns that generate MEG data. However, cortical columns are often curved (Bok, 1929). In future
611 work, the curvature of cortical columns could be approximated using sequences of straight vectors
612 computed from laminar equivolumetric surfaces (Waehnert et al., 2014; Wagstyl et al., 2018). If each

vector was tangential to the corresponding segment of the actual (curved) cortical column, this would result in a piecewise linear estimate of column shape, which may allow more precise source localization (Bonaiuto et al., 2018b, 2018a; Troebinger et al., 2014a). This development would benefit from higher resolution (e.g. 7 Tesla) MRI scans, as well as cytoarchitectonic data from histological sections (Amunts et al., 2013; Wagstyl et al., 2018). The current paper provides a novel framework and set of baselines for *in vivo* evaluation of the impact of future columnar models on source modeling.

Our results are likely to impact other methods which require accurate estimation of cortical surfaces and the orientation of surface normal vectors. For example, current flow modelling techniques that estimate the distribution of current delivered with non-invasive brain stimulation approaches such as transcranial direct current stimulation (tDCS; Bestmann and Walsh, 2017; Bestmann and Ward, 2017) estimate the normal component of the electric field across the cortical surface, and relate this component to the observed physiological changes elicited by tDCS (e.g. Laakso et al., 2019; Seo and Jun, 2019). We expect that improved surface segmentation approaches and vector estimation, as introduced in our present study, will provide more accurate estimates of these normal components. This will be relevant for explaining how current delivery via tDCS impacts on physiological and behavioral responses, and whether the normal component of the electric field is indeed important to explain these effects.

Conclusion

Based on the results of our model comparisons, we have shown that, for evoked responses, source inversion using source locations on the white matter surface and dipole orientation priors computed using link vectors outperforms the other source location and orientation computation methods we tested. We therefore recommend that this approach be used as the default in source inversion.

Acknowledgements

FA, MF, and MB were supported by the European Union's Seventh Framework Programme (FP7/2007–2013)/ERC starting grant agreement number 716862 to M. Bonnefond. KW was supported by the Wellcome Trust (215901/Z/19/Z). The Wellcome Centre for Human Neuroimaging is supported by a strategic award from Wellcome (091593/Z/10/Z). The funders had no role in the preparation of the manuscript.

References

Adjamian, P., Barnes, G.R., Hillebrand, A., Holliday, I.E., Singh, K.D., Furlong, P.L., Harrington, E., Barclay, C.W., Route, P.J.G., 2004. Co-registration of magnetoencephalography with magnetic resonance imaging using bite-bar-based fiducials and surface-matching. Clin. Neurophysiol. 115, 691–8. https://doi.org/10.1016/j.clinph.2003.10.023

Amunts, K., Lepage, C., Borgeat, L., Mohlberg, H., Dickscheid, T., Rousseau, M.-E., Bludau, S., Bazin, P.-L., Lewis, L.B., Oros-Peusquens, A.-M., Shah, N.J., Lippert, T., Zilles, K., Evans, A.C., 2013. BigBrain: An Ultrahigh-Resolution 3D Human Brain Model. Science (80-.). 340, 1472–1475. https://doi.org/10.1126/science.1235381

Baillet, S., 2017. Magnetoencephalography for brain electrophysiology and imaging. Nat. Neurosci. 20, 327–339. https://doi.org/10.1038/nn.4504

Baillet, S., Mosher, J.C., Leahy, R.M., 2001. Electromagnetic brain mapping. IEEE Signal Process. Mag. 18, 14–30. https://doi.org/10.1109/79.962275

Bastos, A.M., Vezoli, J., Bosman, C.A., Schoffelen, J.-M., Oostenveld, R., Dowdall, J.R., De Weerd, P., Kennedy, H., Fries, P., 2015. Visual areas exert feedforward and feedback influences through distinct frequency channels. Neuron 85, 390–401. https://doi.org/10.1016/j.neuron.2014.12.018

Belardinelli, P., Ortiz, E., Barnes, G.R., Noppeney, U., Preissl, H., 2012. Source reconstruction accuracy of MEG and EEG Bayesian inversion approaches. PLoS One 7, e51985. https://doi.org/10.1371/journal.pone.0051985

Berg, P., Scherg, M., 1994. A multiple source approach to the correction of eye artifacts. Electroencephalogr. Clin. Neurophysiol. 90, 229–241. https://doi.org/10.1016/0013-4694(94)90094-9

Bestmann, S., Walsh, V., 2017. Transcranial electrical stimulation. Curr. Biol. 27, R1258–R1262. https://doi.org/10.1016/J.CUB.2017.11.001

Bestmann, S., Ward, N., 2017. Are current flow models for transcranial electrical stimulation fit for purpose? Brain Stimul. 10, 865–866. https://doi.org/10.1016/j.brs.2017.04.002

Bok, S., 1929. Der Einfluss in den Furchen und Windungen auftretenden Krümmungen der Grosshirnrinde auf die Rindenarchitektur. Zeitschrift für die gesamte Neurol. und Psychiatr. 121, 682–750.

Bonaiuto, J., Meyer, S.S., Little, S., Rossiter, H., Callaghan, M.F., Dick, F., Barnes, G.R., Bestmann, S.,

671 2018a. Lamina-specific cortical dynamics in human visual and sensorimotor cortices. Elife 7,
672 226274. https://doi.org/10.7554/eLife.33977

673 Bonaiuto, J., Rossiter, H.E., Meyer, S.S., Adams, N., Little, S., Callaghan, M.F., Dick, F., Bestmann, S.,
674 Barnes, G.R., 2018b. Non-invasive laminar inference with MEG: Comparison of methods and source
675 inversion algorithms. Neuroimage 167, 372–383.
676 https://doi.org/10.1016/j.neuroimage.2017.11.068

677 Boto, E., Holmes, N., Leggett, J., Roberts, G., Shah, V., Meyer, S.S., Muñoz, L.D., Mullinger, K.J., Tierney,
678 T.M., Bestmann, S., Barnes, G.R., Bowtell, R., Brookes, M.J., 2018. Moving
679 magnetoencephalography towards real-world applications with a wearable system. Nature 555,
680 657–661. https://doi.org/10.1038/nature26147

681 Boto, E., Meyer, S.S., Shah, V., Alem, O., Knappe, S., Kruger, P., Fromhold, T.M., Lim, M., Glover, P.M.,
682 Morris, P.G., Bowtell, R., Barnes, G.R., Brookes, M.J., 2017. A new generation of
683 magnetoencephalography: Room temperature measurements using optically-pumped
684 magnetometers. Neuroimage 149, 404–414. https://doi.org/10.1016/j.neuroimage.2017.01.034

685 Buffalo, E.A., Fries, P., Landman, R., Buschman, T.J., Desimone, R., 2011. Laminar differences in gamma
686 and alpha coherence in the ventral stream. Proc. Natl. Acad. Sci. U. S. A. 108, 11262–7.
687 https://doi.org/10.1073/pnas.1011284108

688 Buzsáki, G., Anastassiou, C.A., Koch, C., 2012. The origin of extracellular fields and currents — EEG , ECoG
689 , LFP and spikes 13, 407–420. https://doi.org/10.1038/nrn3241

690 Callaghan, M.F., Josephs, O., Herbst, M., Zaitsev, M., Todd, N., Weiskopf, N., 2015. An evaluation of
691 prospective motion correction (PMC) for high resolution quantitative MRI. Front. Neurosci. 9, 97.
692 https://doi.org/10.3389/fnins.2015.00097

693 Carey, D., Caprini, F., Allen, M., Lutti, A., Weiskopf, N., Rees, G., Callaghan, M.F., Dick, F., 2017.
694 Quantitative MRI Provides Markers Of Intra-, Inter-Regional, And Age-Related Differences In Young
695 Adult Cortical Microstructure. bioRxiv. https://doi.org/https://doi.org/10.1101/139568

696 Dale, A.M., Fischl, B., Sereno, M.I., 1999. Cortical Surface-Based Analysis: I. Segmentation and Surface
697 Reconstruction. Neuroimage 9, 179–194. https://doi.org/10.1006/nimg.1998.0395

698 Dale, A.M., Sereno, M.I., 1993. Improved Localizadon of Cortical Activity by Combining EEG and MEG
699 with MRI Cortical Surface Reconstruction: A Linear Approach. J. Cogn. Neurosci. 5, 162–176.
700 https://doi.org/10.1162/jocn.1993.5.2.162

701 Darvas, F., Pantazis, D., Kucukaltun-Yildirim, E., Leahy, R.M., 2004. Mapping human brain function with
702 MEG and EEG: methods and validation. Neuroimage 23, S289–S299.
703 https://doi.org/10.1016/J.NEUROIMAGE.2004.07.014

704 Fischl, B., 2012. FreeSurfer. Neuroimage 62, 774–781.
705 https://doi.org/10.1016/j.neuroimage.2012.01.021

706 Fischl, B., Sereno, M.I., 2018. Microstructural parcellation of the human brain. Neuroimage 182, 219–
707 231. https://doi.org/10.1016/J.NEUROIMAGE.2018.01.036

708 Friston, K., Harrison, L., Daunizeau, J., Kiebel, S., Phillips, C., Trujillo-Barreto, N., Henson, R., Flandin, G.,
709 Mattout, J., 2008. Multiple sparse priors for the M/EEG inverse problem. Neuroimage 39, 1104–
710 1120.

711 Friston, K., Mattout, J., Trujillo-Barreto, N., Ashburner, J., Penny, W., 2007. Variational free energy and
712 the Laplace approximation. Neuroimage 34, 220–34.
713 https://doi.org/10.1016/j.neuroimage.2006.08.035

714 Fuchs, M., Wagner, M., Wischmann, H.-A., Ottenberg, K., Dössel, O., 1994. Possibilities of Functional
715 Brain Imaging Using a Combination of MEG and MRT, in: Oscillatory Event-Related Brain Dynamics.
716 Springer US, Boston, MA, pp. 435–457. https://doi.org/10.1007/978-1-4899-1307-4_31

717 Fukushima, M., Yamashita, O., Kanemura, A., Ishii, S., Kawato, M., Sato, M., 2012. A State-Space
718 Modeling Approach for Localization of Focal Current Sources From MEG. IEEE Trans. Biomed. Eng.
719 59, 1561–1571. https://doi.org/10.1109/TBME.2012.2189713

720 Goldenholz, D.M., Ahlfors, S.P., Hämäläinen, M.S., Sharon, D., Ishitobi, M., Vaina, L.M., Stufflebeam,
721 S.M., 2009. Mapping the signal-to-noise-ratios of cortical sources in magnetoencephalography and
722 electroencephalography. Hum. Brain Mapp. 30, 1077–1086. https://doi.org/10.1002/hbm.20571

723 Gross, J., Baillet, S., Barnes, G.R., Henson, R.N., Hillebrand, A., Jensen, O., Jerbi, K., Litvak, V., Maess, B.,
724 Oostenveld, R., Parkkonen, L., Taylor, J.R., van Wassenhove, V., Wibral, M., Schoffelen, J.-M., 2013.
725 Good practice for conducting and reporting MEG research. Neuroimage 65, 349–63.
726 https://doi.org/10.1016/j.neuroimage.2012.10.001

727 Haegens, S., Barczak, A., Musacchia, G., Lipton, M.L., Mehta, A.D., Lakatos, P., Schroeder, C.E., 2015.
728 Laminar Profile and Physiology of the α Rhythm in Primary Visual, Auditory, and Somatosensory
729 Regions of Neocortex. J. Neurosci. 35.

730 Hämäläinen, M., Hari, R., 2002. Magnetoencephalographic (MEG) characterization of dynamic brain
731 activation, in: A. Toga and J. Mazziotta (Ed.), Brain Mapping: The Methods. Academic Press,
732 Amsterdam, pp. 227–254.

733 Hämäläinen, M., Ilmoniemi, R., 1984. Interpreting measured magnetic fields of the brain: estimates of
734 current distributions. Tech. rep, Helsinki Univ. Technol.

735 Hämäläinen, M.S., Ilmoniemi, R.J., 1994. Interpreting magnetic fields of the brain: minimum norm
736 estimates. Med. Biol. Eng. Comput. 32, 35–42. https://doi.org/10.1007/BF02512476

737 Haufe, S., Tomioka, R., Dickhaus, T., Sannelli, C., Blankertz, B., Nolte, G., Müller, K.-R., 2011. Large-scale
738 EEG/MEG source localization with spatial flexibility. Neuroimage 54, 851–859.
739 https://doi.org/10.1016/J.NEUROIMAGE.2010.09.003

740 Henson, R.N., Mattout, J., Phillips, C., Friston, K.K.J., 2009. Selecting forward models for MEG source-
741 reconstruction using model-evidence. Neuroimage 46, 168–176.
742 https://doi.org/10.1016/j.neuroimage.2009.01.062

743 Hillebrand, A., Barnes, G.R., 2003. The use of anatomical constraints with MEG beamformers.
744 Neuroimage 20, 2302–13.

745 Hillebrand, A., Barnes, G.R., 2002. A quantitative assessment of the sensitivity of whole-head MEG to
746 activity in the adult human cortex. Neuroimage 16, 638–650.

747 Holmes, N., Leggett, J., Boto, E., Roberts, G., Hill, R.M., Tierney, T.M., Shah, V., Barnes, G.R., Brookes,
748 M.J., Bowtell, R., 2018. A bi-planar coil system for nulling background magnetic fields in scalp
749 mounted magnetoencephalography. Neuroimage 181, 760–774.
750 https://doi.org/10.1016/J.NEUROIMAGE.2018.07.028

751 Iivanainen, J., Stenroos, M., Parkkonen, L., 2017. Measuring MEG closer to the brain: Performance of on-
752 scalp sensor arrays. Neuroimage 147, 542–553.
753 https://doi.org/10.1016/J.NEUROIMAGE.2016.12.048

754 Iivanainen, J., Zetter, R., Grön, M., Hakkarainen, K., Parkkonen, L., 2019. On-scalp MEG system utilizing
755 an actively shielded array of optically-pumped magnetometers. Neuroimage 194, 244–258.
756 https://doi.org/10.1016/J.NEUROIMAGE.2019.03.022

757 Knappe, S., Sander, T., Trahms, L., 2014. Optically-Pumped Magnetometers for MEG, in:
758 Magnetoencephalography. Springer Berlin Heidelberg, Berlin, Heidelberg, pp. 993–999.
759 https://doi.org/10.1007/978-3-642-33045-2_49

760 Laakso, I., Mikkonen, M., Koyama, S., Hirata, A., Tanaka, S., 2019. Can electric fields explain inter-
761 individual variability in transcranial direct current stimulation of the motor cortex? Sci. Rep. 9, 626.
762 https://doi.org/10.1038/s41598-018-37226-x

763 Lin, F.-H., Belliveau, J.W., Dale, A.M., Hämäläinen, M.S., 2006. Distributed current estimates using
764 cortical orientation constraints. Hum. Brain Mapp. 27, 1–13. https://doi.org/10.1002/hbm.20155

765 Little, S., Bonaiuto, J., Barnes, G.R., Bestmann, S., 2018. Motor cortical beta transients delay movement
766 initiation and track errors. bioRxiv 384370. https://doi.org/10.1101/384370

767 López, J.D., Litvak, V., Espinosa, J.J., Friston, K., Barnes, G.R., 2014. Algorithmic procedures for Bayesian
768 MEG/EEG source reconstruction in SPM. Neuroimage 84, 476–487.
769 https://doi.org/10.1016/j.neuroimage.2013.09.002

770 Lutti, A., Hutton, C., Finsterbusch, J., Helms, G., Weiskopf, N., 2010. Optimization and validation of
771 methods for mapping of the radiofrequency transmit field at 3T. Magn. Reson. Med. 64, 229–238.
772 https://doi.org/10.1002/mrm.22421

773 Lutti, A., Stadler, J., Josephs, O., Windischberger, C., Speck, O., Bernarding, J., Hutton, C., Weiskopf, N.,
774 2012. Robust and fast whole brain mapping of the RF transmit field B1 at 7T. PLoS One 7, e32379.
775 https://doi.org/10.1371/journal.pone.0032379

776 Maier, A., Adams, G.K., Aura, C., Leopold, D.A., 2010. Distinct Superficial and deep laminar domains of
777 activity in the visual cortex during rest and stimulation. Front. Syst. Neurosci. 4.
778 https://doi.org/10.3389/fnsys.2010.00031

779 Mattout, J., Henson, R.N., Friston, K.J., 2007. Canonical source reconstruction for MEG. Comput. Intell.
780 Neurosci. 2007, 67613. https://doi.org/10.1155/2007/67613

781 Mattout, J., Phillips, C., Penny, W.D., Rugg, M.D., Friston, K.J., 2006. MEG source localization under
782 multiple constraints: an extended Bayesian framework. Neuroimage 30, 753–67.
783 https://doi.org/10.1016/j.neuroimage.2005.10.037

784 Meyer, S.S., Bonaiuto, J., Lim, M., Rossiter, H., Waters, S., Bradbury, D., Bestmann, S., Brookes, M.,
785 Callaghan, M.F.M.F.M.F., Weiskopf, N., Barnes, G.R., 2017. Flexible head-casts for high spatial
786 precision MEG. J. Neurosci. Methods 276, 38–45. https://doi.org/10.1016/j.jneumeth.2016.11.009

787 Murakami, S., Okada, Y., 2006. Contributions of principal neocortical neurons to
788 magnetoencephalography and electroencephalography signals. J. Physiol. 575, 925–936.
789 https://doi.org/10.1113/jphysiol.2006.105379

790 Nolte, G., 2003. The magnetic lead field theorem in the quasi-static approximation and its use for
791 magnetoenchephalography forward calculation in realistic volume conductors. Phys. Med. Biol. 48,
792 3637–3652. https://doi.org/10.1088/0031-9155/48/22/002

793 Nunez, P., Srinivasan, R., 2006. Electric fields of the brain: the neurophysics of EEG. Oxford University
794 Press.

795 Okada, Y.C., Wu, J., Kyuhou, S., 1997. Genesis of MEG signals in a mammalian CNS structure.
796 Electroencephalogr. Clin. Neurophysiol. 103, 474–85.

797 Penny, W.D., Stephan, K.E., Daunizeau, J., Rosa, M.J., Friston, K.J., Schofield, T.M., Leff, A.P., 2010.
798 Comparing families of dynamic causal models. PLoS Comput. Biol. 6, e1000709.
799 https://doi.org/10.1371/journal.pcbi.1000709

800 Ross, B., Charron, R.E.M., Jamali, S., 2011. Realignment of Magnetoencephalographic Data for Group
801 Analysis in the Sensor Domain. J. Clin. Neurophysiol. 28, 190–201.
802 https://doi.org/10.1097/WNP.0b013e3182121843

803 Salmelin, R., Hämäläinen, M., Kajola, M., Hari, R., 1995. Functional segregation of movement-related
804 rhythmic activity in the human brain. Neuroimage 2, 237–43.

805 Seo, H., Jun, S.C., 2019. Relation between the electric field and activation of cortical neurons in
806 transcranial electrical stimulation. Brain Stimul. 12, 275–289.
807 https://doi.org/10.1016/J.BRS.2018.11.004

808 Singh, K.D., Holliday, I.E., Furlong, P.L., Harding, G.F.A., 1997. Evaluation of MRI-MEG/EEG co-registration
809 strategies using Monte Carlo simulation. Electroencephalogr. Clin. Neurophysiol. 102, 81–85.
810 https://doi.org/10.1016/S0921-884X(96)96570-4

811 Spaak, E., Bonnefond, M., Maier, A., Leopold, D.A., Jensen, O., 2012. Layer-specific entrainment of γ-
812 band neural activity by the α rhythm in monkey visual cortex. Curr. Biol. CB 22, 2313–2318.
813 https://doi.org/10.1016/j.cub.2012.10.020

814 Stolk, A., Todorovic, A., Schoffelen, J.-M., Oostenveld, R., 2013. Online and offline tools for head
815 movement compensation in MEG. Neuroimage 68, 39–48.
816 https://doi.org/10.1016/J.NEUROIMAGE.2012.11.047

817 Troebinger, L., López, J.D., Lutti, A., Bestmann, S., Barnes, G.R., 2014a. Discrimination of cortical laminae
818 using MEG. Neuroimage 102, 885–893. https://doi.org/10.1016/j.neuroimage.2014.07.015

819 Troebinger, L., López, J.D., Lutti, A., Bradbury, D., Bestmann, S., Barnes, G.R., 2014b. High precision
820 anatomy for MEG. Neuroimage 86, 583–91. https://doi.org/10.1016/j.neuroimage.2013.07.065

821 van Kerkoerle, T., Self, M.W., Dagnino, B., Gariel-Mathis, M.-A., Poort, J., van der Togt, C., Roelfsema,
822 P.R., 2014. Alpha and gamma oscillations characterize feedback and feedforward processing in
823 monkey visual cortex. Proc. Natl. Acad. Sci. U. S. A. 111, 14332–14341.
824 https://doi.org/10.1073/pnas.1402773111

825 Waehnert, M.D., Dinse, J., Weiss, M., Streicher, M.N., Waehnert, P., Geyer, S., Turner, R., Bazin, P.-L.,
826 2014. Anatomically motivated modeling of cortical laminae. Neuroimage 93, 210–220.

827 Wager, T.D., Keller, M.C., Lacey, S.C., Jonides, J., 2005. Increased sensitivity in neuroimaging analyses
828 using robust regression. Neuroimage 26, 99–113.

https://doi.org/10.1016/J.NEUROIMAGE.2005.01.011

Wagstyl, K., Lepage, C., Bludau, S., Zilles, K., Fletcher, P.C., Amunts, K., Evans, A.C., 2018. Mapping Cortical Laminar Structure in the 3D BigBrain. Cereb. Cortex 28, 2551–2562. https://doi.org/10.1093/cercor/bhy074

Weiskopf, N., Suckling, J., Williams, G., Correia, M.M., Inkster, B., Tait, R., Ooi, C., Bullmore, E.T., Lutti, A., 2013. Quantitative multi-parameter mapping of R1, PD(*), MT, and R2(*) at 3T: a multi-center validation. Front. Neurosci. 7, 95. https://doi.org/10.3389/fnins.2013.00095

Whalen, C., Maclin, E.L., Fabiani, M., Gratton, G., 2008. Validation of a method for coregistering scalp recording locations with 3D structural MR images. Hum. Brain Mapp. 29, 1288–1301. https://doi.org/10.1002/hbm.20465

Wipf, D., Nagarajan, S., 2009. A unified Bayesian framework for MEG/EEG source imaging. Neuroimage 44, 947–966. https://doi.org/10.1016/J.NEUROIMAGE.2008.02.059